Ground-based remote sensing of aerosol properties using high resolution infrared emission and Lidar observations in the high Arctic

Denghui Ji[1], Mathias Palm[1], Christoph Ritter[2], Philipp Richter[1], Xiaoyu Sun[1], Matthias Buschmann[1], and Justus Notholt[1]

[1]Institute of Environmental Physics, University of Bremen, Otto-Hahn-Allee 1, 28359 Bremen, Germany
[2]Alfred Wegener Institute, Helmholtz Centre for Polar and Marine Research, Telegrafenberg A43, 14473 Potsdam, Germany

Correspondence: Denghui Ji (denghui_ji@iup.physik.uni-bremen.de)

Abstract. Arctic amplification, the phenomenon that the Arctic is warming faster than the global mean, is still not fully understood. The Transregional Collaborative Research Centre TR 172 – Arctic Amplification: Climate Relevant Atmospheric and Surface Processes (AC)[3] funded by the DFG (German research foundation) ~~contribute~~ contributes towards this research topic. For the purpose of measuring aerosol components, a Fourier-Transform ~~InfraRed spectrometer~~ Infrared Spectrometer (FTS) for measuring down-welling emission since 2019 and a Raman-Lidar are operated at the AWIPEV research base in Ny-Ålesund, Spitsbergen (79 °N, 12 °E). To do aerosol retrieval using measurements from the FTS, a retrieval algorithm based on the Line-by-Line Radiative Transfer Model and DIScrete Ordinate Radiative Transfer model (LBLDIS), is modified for different aerosol types (dust, sea salt, black carbon, and sulfate), aerosol optical depth (AOD) and effective radius (R_{eff}). Using Lidar measurement, an aerosol and cloud classification method is developed for providing basic information about the distribution of aerosols or clouds in the atmosphere and used as an indicator to ~~do aerosols or clouds retrieval in~~ perform aerosol or cloud retrievals using the FTS. Therefore, a two-instruments joint observation scheme is designed and is performing on the data measured from 2019 to present. In order to show this measurement technique in details, ~~two case studies are selected, one is~~ a case study for an aerosol-only case ~~on~~ is presented with data from the 10th of June ~~2020 and the another is a cloud-only case on 11th of June~~ 2020. In the aerosol-only case, the retrieval results show that sulfate ($\tau_{900cm^{-1}}$=0.007 $\pm$ 0.0027) is the dominant aerosol during the whole day, followed by dust ($\tau_{900cm^{-1}}$=0.0039 $\pm$ 0.0029) and black carbon ($\tau_{900cm^{-1}}$=0.0017 $\pm$ 0.0007). Sea salt ($\tau_{900cm^{-1}}$=0.0012 $\pm$ 0.0002)~~shows the lowest AOD value as its~~ , which has the weakest emission ability in ~~infrared waveband~~the infrared waveband, shows the lowest AOD value. Such proportions of sulfate, dust and BC also show good agreement with MERRA-2 reanalysis data. ~~Besides, comparing with~~ Additionally, the comparison with a sun-photometer (AERONET) ~~,~~ shows the daily variation of aerosol AOD retrieved from FTS ~~is~~ to be similar with that ~~in~~ of the sun-photometer. ~~In the cloud-only case study, Lidar distinguishes the cloud signal from aerosols accurately, giving a very good information on the state of the atmosphere. For showing the importance of Lidar measurement in the retrieval of FTS, two versions of retrieval algorithm, one for cloud retrieval and another for aerosols retrieval are applied for gaining cloud parameters and aerosol parameters respectively. The result shows that without information from Lidar measurement, the signal of cloud is misunderstood and retrieved as four aerosols in FTS, which indicates that the combination of both measurements is necessary~~

and helpful in our aerosol retrievalUsing this method, long time period observations from April to August in 2020 are retrieved and presented. Sulfate is often present in the Arctic. It is higher in Spring and lower in Summer. Similarly, BC is also frequently observed in the Arctic, with less obvious seasonal variations than sulfate. A BC outburst event is observed in each Spring and Summer. In spring, sulfate and BC are dominant while sea salt and dust are relatively low. In addition, a sea salt enhancement event is observed in Summer time, which might be due to the melting of sea ice and emitted from nearby open water. From the retrieved results in long time period, none of them show a clear correlation, so they can be retrieved independent of each other.

1 Introduction

In the Arctic, near surface temperatures are rising much faster than those of the global mean (Wendisch et al., 2017). This phenomenon is called Arctic Amplification (Serreze and Barry, 2011; Wendisch et al., 2017; Previdi et al., 2021). In order to understand the causes and effects of the rapid warming in the Arctic, many studies focus on key processes contributing to Arctic amplification, like temperature feedback (Bony et al., 2006; Soden and Held, 2006), surface albedo feedback (Graversen et al., 2014) and cloud and water vapor feedback (Taylor et al., 2013; Philipp et al., 2020). The cooperative research programm collaborative research program TR 172 (AC)^3 focuses on the Arctic Amplification[1].

Apart from the physical feedback processes, aerosol has a large impact on the Arctic environment (Abbatt et al., 2019; Schmale et al., 2021). Aerosol influences the Arctic climate by aerosol-cloud interactions (Fan et al., 2016) and aerosol-surface interactions (Donth et al., 2020). For example, Black Carbon (BC) deposits on snow and ice, lowering the surface albedo (Ming et al., 2009; Bond et al., 2013) and thus warming the surface. Dust, when present in layers over high albedo surfaces and/or deposited to the snow, will warm the atmosphere (Krinner et al., 2006); Sulfate, organic matter and sea salt may cool the Arctic by scattering light back to space and by modifying the microphysics of liquid clouds (Schmeisser et al., 2018). At cirrus temperatures, dust, ammonium sulfate and sea salt increase the cloud albedo by increasing ice crystal concentrations (Wagner et al., 2018).

In recent decades, there were mainly in-situ measurements of aerosols were performed in the Arctic. Most reports show that the aerosol composition is changing. Koch et al. (2011) and Ren et al. (2020) find that sulfate and BC are decreasing compared to the last century. Several projects in (AC)^3 also focuses focus on BC concentration measurements (Kodros et al., 2018; Zanatta et al., 2018) and reveal the annual cycle of BC in the Arctic, higher in spring and lower in early summer (Schulz et al., 2019). Shaw (1995), Francis et al. (2018), Francis et al. (2019) find that dust can be transported over long distances into the Arctic and plays an important role in Arctic haze. In recent years, the area of open water becomes has become larger, and the sea surface temperature is increasing, which leads to a local increase of the emission of sea salt (Domine et al., 2004; Struthers et al., 2011; May et al., 2016). Thus, during the Arctic warming period, the proportions of different aerosols in the Arctic could also change.

There are several ways to measure the aerosol composition, such as remote sensing from satellite or ground-based instruments, in-situ measurement on the surface or from aircraft. Satellite instruments can provide measurements of large areas

[1] www.ac3-tr.de

but are not very suitable in the Arctic due to the frequent existence of clouds and snow/ice on the surface, which make the measurements challenging (Lee et al., 2021). The in-situ measurements provide much more accurate measurements, but are often limited to the planetary boundary layer~~and a distinct position. The ground-based remote sensing method avoids the disturbance~~ , have limited coverage and are sparse in time. Ground-based remote sensing provides measurements with a similar measurement geometry than satellites which are not confined to a particular altitude, unlike in-situ measurements. They provide time series measurements from the surface and has a similar viewing geometry as the satellite. Hence, a combination of different measurement methods is necessary to provide a complete picture of aerosols in the Arctic. In this paper, we focus on ~~the~~ a passive ground-based remote sensing method in the thermal infrared to retrieve the aerosol components. Using atmospheric thermal emission spectra, measured by a Fourier Transform spectrometer (FTS), we perform a retrieval of aerosol properties as proposed by Rathke et al. (2002). Turner (2008) extended this method to dust measurements. Previous studies (Rathke et al., 2002; Turner, 2008) are limited to a specific type of aerosol, such as sulfate or dust. Based on them, this paper will further expand the number of aerosol types that can be measured by FTS.

In section 2, the location of measurement site and the setup of two instruments ~~is~~ are described. Section 3 presents the joint observation scheme using two instruments (Lidar KARL and the Fourier Transform spectrometer, NYAEM-FTS) and information of the retrieval algorithm for NYAEM-FTS, including details of look-up tables of aerosol scattering properties. Section 4 shows the results of both KARL and NYAEM-FTS measurements in ~~two case studies on~~ one case study of an aerosol-only event (10th June 2020) and ~~cloud-only event (11th June 2020).~~ long time period observation from April to August in 2020. The article ends with a summary and conclusion in section 5.

2 Location and Instruments Description

2.1 Site description

Ny-Ålesund (79 °N, 12 °E), Svalbard, is located in the North Atlantic atmospheric transport gateway to the Arctic. The AWIPEV[2] research base is part of the village Ny-Ålesund, jointly operated by the AWI Potsdam[3] and the IPEV institute[4].The AWI Potsdam operates an extensive suite of instruments, some of which are a very useful ~~combination~~ complement to the NYAEM-FTS (section 2.2), including an aerosol Lidar instrument (section 2.3) and a sun-photometer (~~appendix~~ section 3.2).

2.2 The NYAEM-FTS ~~Measurement~~Instrument

The Fourier Transform spectrometer, NYAEM-FTS, for measuring down-welling emission in the thermal infrared was installed in summer 2019. The NYAEM-FTS consists of a Bruker Vertex 80 Fourier Transform Spectrometer, a SR800 blackbody, an automatically operated mirror to select the radiation source and an automatically operated hutch with shields the instrument from the environment. It is situated in a temperature stabilized laboratory, at about 21 - 25 °C.

[2]www.awipev.eu
[3]Alfred Wegener Institut; www.awi.de
[4]Polar Institute Paul Emile Victor; www.ipev.fr

The Bruker Vertex 80 instrument is a table-top instrument. It is operated in zenith geometry with an adjustable field of view in the range of 3.3 to 22 mrad. The beamsplitter is a KBr beam splitter and the detector is an extended MCT detector with the spectral range 400 - 2500 cm^{-1} (4 - 25 µm). This instrument measures with a spectral resolution of 0.08 cm^{-1} (08.2019 - 08.2020) and 0.3 cm^{-1} (08.2020 to present). ~~Spectra in different resolutions are all suitablefor aerosol retrieval~~For the analysis of aerosol properties all resolutions are suitable, because the spectral features are broadband (compare Fig. 1). The mirror selecting the emission source is the first optical part of the setup, and a total power calibration is performed to gain the radiance from spectra (Revercomb et al., 1988). This means three measurements are required to complete the observation of a spectrum, two measurements of the blackbody ~~in~~ at hot and ambient temperature respectively, and one measurement pointing skywards (Rathke and Fischer, 2000; Turner, 2005; Richter et al., 2022). The SR800 blackbody is used as a blackbody radiator. It can be adjusted between 0 and 120 °C, holding the temperature within 0.1 K.

~~Figure~~Fig. 1 shows four different emission spectra measured by the NYAEM-FTS in clear day, thick cloud, thin cloud and aerosol event respectively. The Planck function at 280 K is also presented in this figure. From Fig. 1, the intensity of thick cloud emission in infrared is high, close to the one calculated from Planck function. ~~Compared with thick cloud,~~ However, in the atmospheric window between 800 - 1200 cm^{-1}~~in the emission spectrum in clear day is obvious and~~ , the intensity of ~~the spectral baseline is~~ clear sky emission is quite lower (close to zero) than that in thick cloud. Between the emission spectra of thick cloud and clear ~~day~~ sky in this window (800 - 1200 cm^{-1}), an aerosol (Fig. 1 orange line) and a thin cloud (Fig. 1 blue line) emission spectra are presented as well, showing the baseline, from which the aerosol information will be retrieved. In general, it is easy to distinguish the difference between a spectrum of ~~thick cloud with a spectrum in clear day~~a thick cloud and a clear sky spectrum, however, distinguishing aerosols from a thin cloud is difficult or impossible. ~~Therefor~~ Therefore more information from other instruments, e.g. Lidar measurement is used to distinguish days with clouds from days with aerosols present above the instrument.

2.3 The Raman-Lidar "KARL"

In ~~Ny Ålesund~~Ny-Ålesund, a Raman-Lidar "KARL" is operated to measure in 3 colors (355, 532, and 1064 nm) (Ritter et al., 2016). It is positioned about 10 meters away from NYAEM-FTS measurement also pointing skywards. Aerosol backscatter coefficients (in all three colors), extinction coefficients (355 and 532 nm), and depolarization (355 and 532 nm) are measured.

For Lidar products, the aerosol backscatter coefficient (β^{aer}), the aerosol depolarization (δ^{aer}) and the color ratio (CR) are used for aerosol optical property analysis. According to Freudenthaler et al. (2009), the definitions of those quantities are given as follows:

$$\delta^{aer}(\lambda) = \frac{\beta_{\perp}^{aer}(\lambda)}{\beta_{\parallel}^{aer}(\lambda)} \tag{1}$$

$\beta_{\perp}^{aer}(\lambda)$ and $\beta_{\parallel}^{aer}(\lambda)$ are the backscatter coefficients of the vertical and parallel polarized light, respectively. The depolarization depends on the particles' shape, e.g. spherical particles do not show any depolarization in the backscatter.

$$CR(\lambda_1, \lambda_2) = \frac{\beta_{\lambda_1}^{aer}}{\beta_{\lambda_2}^{aer}} \tag{2}$$

β_{λ}^{aer} is the aerosol backscatter coefficient at wavelength λ.

~~The definitions of those parameters and more~~ More details are given in Freudenthaler et al. (2009) and Ritter et al. (2016). Based on that, Ritter et al. (2016) distinguished six conditions for the aerosol classification using those Lidar quantities (compare Tab. 1).

3 Methods and Data

3.1 ~~Instruments Joint Observation SchemeAs we~~ Retrieval Algorithm TCWRET2-V1 and TCWRET-V2

The retrieval algorithms, TCWRET-V1 and TCWRET-V2, are based on TCWRET developed by Richter et al. (2022). TCWRET-V1 is used for cloud parameter retrieval while TCWRET-V2 is modified for aerosol retrieval. The main difference between the two is the scattering properties look-up table. The core of the retrieval program TCWRET is the radiative transfer model LBLDIS (Richter et al., 2022) which consists of the clear sky radiative transfer model LBLRTM (Clough et al., 2005) and the scattering code DISORT (Stamnes et al., 1988) . The coupled model LBLDIS is used in several retrieval algorithms, such as MIXCRA (Turner, 2005), CLARRA (Rowe et al., 2013), and TCWRET (Richter et al., 2022). Note that these retrieval algorithms share the same forward models. The differences are the particular implementation, e.g. of the scattering.

In this paper, TCWRET-V1 means TCWRET with cloud databases, while TCWRET-V2 means TCWRET with aerosol databases. The algorithm reliability, or how well the method can precisely retrieve aerosol information, has been tested in section 3.1.2. In the Sec. 3.1.1, the aerosol scattering properties look-up tables and artificial spectra simulated using forward model are described in detail. A description of retrieval algorithm can be found in App. B.

3.1.1 Aerosol Scattering Properties Look-up Tables

In this study, sulfate, sea salt, dust, and BC are retrieved using the retrieval algorithm, TCWRET-V2. The complex refractive index database only covers the above mentioned aerosols in the infrared band because the spectral signature of the other aerosols is too small and it is not possible to retrieve them from the IR spectra. The complex imaginary refractive index of sulfate and dust are based on OPAC/GADA database, BC from Chang and Charalampopoulos (1990), and sea salt from Eldridge and Palik (1997), and Palik (1997) (compare Fig. 3).

The aerosol optical properties are calculated using the Lorenz-Mie theory. The code for this calculation has been developed by Mishchenko et al. (1999). For aerosol scattering properties calculations, information on the aerosol size distribution as well as their shapes is also needed. In Mie code (Mishchenko et al., 1999), the sphere shape of aerosol with a single-mode log-normal size distribution of particles is selected. The log-normal function is given as follows:

$$n_N(D) = \frac{N}{\sqrt{2\pi D ln(\sigma_g)}} exp(-\frac{ln^2(D/D_g)}{ln^2(\sigma)}) \quad (3)$$

Where N is the total aerosol number concentration D_g is the median diameter, and σ_g is termed geometric standard deviation. In this study, the geometric standard deviation of size distribution of aerosol is assumed to be 0.2 and the effective radius (R_{eff})

is set from 0.1 to 1 μm. The main reason for setting the upper limit of the R_{eff} to 1 μm is that aerosols in the Arctic region is often below 1 μm, according to the measurements of aerosol size distribution in the Arctic area ((Asmi et al., 2016; Park et al., 2020; Boyer et al.,). In addition, if such constraint is not set to 1 μm, occasionally, the retrieval of fine particles, such as sulfate and BC, will be mathematically increased for a better fit of the spectrum, which is artificial. Because sea salt can be larger than 1 μm, when the retrieved R_{eff} of sea salt is close to 1 μm and sea salt is the dominant aerosol, the database of sea salt is extended to 2.5 μm and the retrieval is run again.

3.1.2 Instruments Joint Observation Scheme

As previously indicated, it is difficult to distinguish between thin clouds and aerosols only relying on the NYAEM-FTS instrument. To select the spectra in aerosol-only scenarios, the measurements of the KARL Lidar are used (compare Sec. 2.3).

~~First, the presence and distribution of clouds or aerosols are distinguished using the Lidar classification method (Sec. 2.3).~~ The aerosol or cloud height ~~can also be determined by Lidar and fixed in the retrieval algorithm for the FTS retrieval algorithm~~is determined from the KARL Lidar measurement and provided to the retrieval algorithm, TCWRET (compare Sec. 3.1). For cloud-only observations, the first version of retrieval algorithm, Total Cloud Water retrieval (~~TCWret-V1), will be used to do cloud parameters retrieval, which is described in~~ TCWRET-V1), is used to retrieve cloud parameters as described by Richter et al. (2022). For aerosol-only events, the modified version~~of TCWret-V2 will be adopted~~ , TCWRET-V2, is used to do the aerosol components retrieval~~, which will be given in the following section~~. For complex situations ~~of the~~ with simultaneous existence of clouds and aerosols, the concurrent ~~FTS~~ NYAEM-FTS measurements will be excluded~~according to Lidar measurement~~. The flow diagram of ~~instruments~~ the joint observation scheme ~~could be~~ is found in Fig. 2a. ~~Based on the Lidar measurement, NYAEM-FTS will be used for cloud or aerosol retrieval using the corresponding databases for scattering coefficients.~~

The flow diagram in ~~TCWret-V2~~ TCWRET-V2 is given in Fig. 2b. As shown in Fig. 2b, there are ~~four inputs should be prepared for model simulation. First~~several inputs for model simulations. Firstly, the databases for scattering coefficients of different aerosol types are calculated using Mie code (Mishchenko et al., 1999) based on aerosol complex refractive index and aerosol size distribution. ~~Second~~Secondly, the atmospheric state profile, which includes temperature, humidity, and pressure (~~refered~~ referred to as THP), is obtained from ERA5 reanalysis data with a time resolution of 3 hours (Hersbach et al., 2018). The third input ~~of the DISCrete Ordinate Radiative Transfer model (DISORT, Stamnes et al. (1988)) is the optical depth of gases in the whole atmosphere, which is calculated from the Line-by-Line Radiative Rransfer Model (LBLRTM, Clough et al. (2005)), using THP profile that we mentioned before. The last input for DISORT~~ is the aerosol height information, which is provided by the KARL Lidar (Sec. 2.3). To obtain the temperature of the aerosol layer, ~~it is interpolated from~~ the fourth input, the ERA5 temperature ~~data based on the height measured by~~ is interpolated to the altitude measured by the KARL Lidar. Furthermore, for all aerosol types, the ~~apriori~~ a priori information of aerosol is fixed as AOD = 0.0001 and R_{eff} = 0.35 μm. ~~With the preparation of all input data, the model can simulate the spectrum and then use the retrieval algorithm to retrieve the aerosol parameters, trying to making the simulated one closer to the measured one. All of these processes will be explained in detail in the following section.~~

3.2 ~~Retrieval Algorithm in NYAEM-FTS~~

~~The retrieval algorithms, TCWret-V1 and TCWret-V2, are based on TCWret developed by Richter et al. (2022). TCWret-V2 is modified for aerosol retrieval. The main difference between TCWret-V1 and TCWret-V2 is the scattering properties look-up table. Besides, the algorithm reliability, or how well the method can precisely retrieve aerosol information has been tested. In the Sec. 3.1.1, the aerosol scattering properties look-up tables and artificial spectra simulated using forward model are described in detail. The theory of retrieval algorithm can be found in App. **??**.~~

3.1.1 ~~Aerosol Scattering Properties Look-up Tables~~

~~Aerosol types can be categorized in several ways. In this study, sulfate, sea salt, dust, and BC are adopted in the retrieval algorithm. This is consistent with the reanalysis data, such as the MERRA-2 reanalysis data (Gelaro et al., 2017), which is convenient for data comparison. On the other hand, the complex refractive index database only covers the above aerosols in the infrared band. Furthermore, the residual term of spectral fitting is too small to consider other aerosol databases for inversion. The complex imaginary refractive index of sulfate and dust are based on OPAC/GADA database, BC from Chang and Charalampopoulos (19 , and sea salt from Eldridge and Palik (1997), and Palik (1997) (compare Fig. 3).~~

~~Information on aerosol size distribution as well as their shapes is also needed. In this study, we assume that the shape of aerosol is a sphere with a single-mode lognormal size distribution. The infrared spectra do not contain enough information to get real shape information. The width of size distribution of aerosol is assumed to be 0.2 and the effective radius (R_{eff}) is set from 0.1 to 1 . Based on that, aerosol optical properties are calculated using the Lorenz-Mie theory. The code for this calculation has been developed by Mishchenko et al. (1999).~~

3.1.1 Artificial Spectra from LBLDIS

When considering down-welling emission from the atmosphere on a clear day, the main contribution to emission in the thermal infrared band are from the greenhouse gases, i.e. CO_2, H_2O, N_2O, CO, CH_4 and O_3. If there is a ~~layer of~~ cloud or aerosol ~~, the~~ layer, its broad band emissions ~~from cloud and aerosol~~ can be observed as well ~~. In order to model the spectrum, two radiative transfer models are used to simulate the down-welling emission from the atmosphere, one is the Line-by-Line Radiative Rransfer Model (LBLRTM, Clough et al. (2005)) for the gaseous contribution, another is the DIScrete Ordinate Radiative Transfer model (DISORT, Stamnes et al. (1988)) for calculation of scattering of the radiation on water droplets and aerosol particles. The coupled model is called LBLDIS and is used in several retrieval algorithms, such as MIXCRA (Turner, 2005), and CLARRA (Rowe et al., 2013), and TCWret (Richter et al., 2022). Note, all this retrieval algorithms share the same forward models. The differences are the particular implementation, e.g.of the scattering~~(compare Fig. 1).

Several thermal infrared emission spectra from the LBLDIS model are shown in Fig. 4. Under the same number density, different aerosol types exhibit unique characteristics in the infrared emission spectra, shown in Fig. 4a. Among those aerosols, the radiance emitted from sea salt is lowest, due to its ~~small particles~~ smallest light absorbing capability compared to other aerosols. When the number density is fixed in model simulation, the radiance from sea salt increases with the size of particles

(Fig. 4b). Other aerosol types with larger size are presented in Fig. A1. Using the same number density, the radiance from sea salt with the same size as other aerosols is significantly lower; only when sea salt has a large particle size compared to the other aerosols, are the radiances comparable. Figure 4c shows the thermal infrared emission spectra of ~~atmosphere~~ atmospheric gases (clear sky) and different aerosols within atmosphere. According to Fig. 4c, ~~there is no aerosol signal~~ in some wavebands~~due to the domination of~~ , the gas emission dominates over the aerosol signal. Those bands are not considered for the retrieval, e.g. CO_2 in 640 - 690 cm^{-1} and O_3 in 1000 - 1100 cm^{-1}. ~~Apart from those wavebands, the four aerosol signals are obvious especially~~ Aerosol windows (compare Fig. A2) are chosen in the region in 500 - 600 cm^{-1}, 800 - 1000 cm^{-1}, and 1100 - 1200 cm^{-1}, which are selected as retrieval micro-windows (vertical lines in Fig. 4c).~~To make the signatures of aerosols more obvious, the~~ The spectra in Fig. 4d are shown in the form of the difference between the aerosol and clear sky in those micro-windows . Based on that, the emission spectra in aerosol events are different from each other~~and independent~~, which means the emission from aerosols can be measured and aerosol types ~~could~~ can be retrieved using the emission FTS. The reason for avoiding the gas emissions is the dependency of the gas emissions on the temperature distribution in the atmosphere.

3.1.2 Error estimation

In order to investigate the precision of the retrieved values, artificial spectra simulated from LBLDIS are used to explore the performance of ~~TCWret-V2~~ TCWRET-V2 in the retrieval of aerosol types. Artificial spectra with preset values of AOD as well as R_{eff} are created using LBLDIS and then act as measured spectra retrieved by the algorithm. Specifically, we assume that all particles are concentrated on a single level, 2000 m above surface ground. The AOD's of sea salt, sulfate, dust and BC are set 0.1, respectively, with R_{eff} of 0.7 µm. The retrieval results suffer from several uncertainty sources:

- ~~uncertainty~~ Uncertainty of the aerosol height, which is similar to the error of aerosol layer temperature. In this study, the aerosol height is given by Lidar measurement.

- ~~uncertainty~~ Uncertainty of the humidity profile has a significant signal on the far-infrared emission spectrum, at about 1500 - 2000 cm^{-1}. Thus, the ~~uncertainty of~~ water vapor profile could change the radiance of emission spectrum, which might affect the results of retrieval. ~~In the retrieval processes, ERA5 hourly data on pressure levels from 1959 to present is used into retrieval (Hersbach et al., 2018).~~

- ~~Calculation uncertainty in~~ Calibration uncertainty in the measured spectra is also an important uncertainty in the retrieval, which could be caused by ~~non-perfect emission of blackbodies~~misreading of the blackbody temperature. In this study, the total power calibration method (Revercomb et al., 1988) is used to calibrate the spectra. Assuming the accuracy of the blackbody temperature is $\Delta T_{BB} = \pm 1K$. The propagation of this error into radiance is

$$\Delta L = \sqrt{(\frac{\partial L_{atm}}{\partial T_{BB}} \cdot 1K)^2} \tag{4}$$

According to Richter et al. (2022), the partial derivative $\frac{\partial L_{atm}}{\partial T_{BB}}$ can be estimated using:

$$L_{atm} = B(T_{amb}) + 0.2 \cdot (B(T_{hot}) - B(T_{amb})) \tag{5}$$

where $B(T_{hot})$ means hot blackbody temperature and $B(T_{amb})$ means surface air temperature. With $T_{hot} = 100$ °C and $T_{amb} = 0$ °C, $\frac{\partial L_{atm}}{\partial T_{BB}} \cdot 1K = 0.41 \mathrm{mWsr^{-1}m^{-2}cm^{-1}}$ is an average for the spectral interval between 500 and 2000 $\mathrm{cm^{-1}}$.

- ~~Measurement uncertainty is cuased by the noise on the spectral measurements, a random noise due to fluctuations on the detectors~~Measurement uncertainty. The noise on the spectrum is assumed to be white in space and time.

- ~~Databases~~ Database uncertainty could be caused by uncertainty of aerosol complex refractive index. Both the real and imaginary part could have an influence on the accuracy of aerosol scattering properties look-up tables, as we mentioned in Sec. 3.1.1.

The artificial spectra with modifications are performed according Tab. 2. Compared with preset values, one can then compute the difference between retrieved values with preset values by perturbing each parameter~~, as~~.

3.2 AOD in AERONET and MERRA-2

The dataset, AErosol RObotic NETwork (AERONET), provides aerosol products primarily in the visible waveband. Additionally, Modern-Era Retrospective analysis for Research and Applications version 2 (MERRA-2) provides aerosol information. Hence, it is worth investigating whether our measurements can be combined with existing data to provide more comprehensive aerosol information in the future. In this paper, we summarize the results from AERONET and MERRA-2 in the aerosol case for providing a general understanding of the aerosol events (compare Fig. 8).

The AERONET project is a federation of ground-based remote sensing aerosol networks. It is widely used as a ground-based reference for validation of aerosol retrievals. In Ny-Ålesund, a Sun-photometer measuring solar extinction at several wavelengths is adopted to give the daily variance of AOD on 10th of June 2020.

MERRA-2 is the latest version of the global atmospheric reanalysis dataset produced by NASA Global Modeling and Assimilation Office (GMAO) using the Goddard Earth Observing System Model (GEOS) version 5.12.4. An hourly time-averaged 2-dimensional data collection (M2T1NXAER) in MERRA-2 is used in this study (Gelaro et al., 2017). This collection consists of assimilated aerosol diagnostics, such as column mass density of aerosol components (BC, dust, sea salt, sulfate, and organic carbon), surface mass concentration of aerosol components, and total extinction (and scattering) AOD at 550 nm. The dataset covers the period of 1980 to present. In this paper, the AOD of sea salt, sulfate, dust, BC and organic carbon in Ny-Ålesund are shown on 10th of June 2020.

4 Results

4.1 Artificial Spectra Retrieval

As we mentioned in Sec. 3.1.2, the artificial spectra are given by forward model with preset values (compare Tab. 2). The retrieved results of those artificial spectra can be obtained by using the artificial spectra as the observed spectra in the retrieval algorithm. The difference between retrieved values with preset values by perturbing each parameter is shown in Fig. 5.

~~In~~ Fig. 5~~,~~ a shows that the original case~~means ,~~ without any modifications ~~as we mentioned before, which are close to~~ is close to the preset values. The difference of AOD retrieved in the original case with preset values are less than 0.005 at 900 cm^{-1}, ~~meaning~~ leading to convincing results using this retrieval algorithm. ~~Besides, among those modification cases, uncertainties in~~ Noise in the measurements and water vapor profiles have small ~~aeffect~~ effects on the retrieval. The most ~~sensitive parameter is~~ important parameter is the database error, caused by ~~uncertainty of~~ the uncertainty of the complex refractive index. A ~~derease~~ decrease of 10% in the real part of the complex refractive index will cause about 7% positive errors in AOD of sulfate, dust and BC, except for AOD of sea salt, which shows 18% negative error. While the 10% decrease of the imaginary part of the complex refractive index will cause about 4% negative errors in AOD of sulfate, dust and BC and 1% negative error in AOD of sea salt. Following the databases errors, the second most important error is the calibration error, ~~an offset~~ e.g. 1 K misreading of the temperature of the blackbody will cause a change in radiance of about 0.47 $\mathrm{mWsr}^{-1}\mathrm{m}^{-2}\mathrm{cm}^{-1}$. An offset of radiance by 1 $\mathrm{mWsr}^{-1}\mathrm{m}^{-2}\mathrm{cm}^{-1}$ ~~cuases~~ causes an error of about 4% overestimation in ~~results. Temperature error~~ the results. The temperature error of the aerosol layer is the third most important effect in the aerosol retrieval.

In order to show the reliable range of the retrieved AOD, using similar artificial spectra but for several AOD from 0.001 to 0.1 at 900 cm^{-1}, the relative uncertainties of AOD in original cases with those preset values are given in Fig. 5b. The uncertainty of the AOD retrieval is 0.0015, hence aerosols are reliably retrieved when the AOD is > 0.003. Therefore, we consider the results to be reliable when the retrieved AOD is greater than 0.003.

Organic carbon (OC) is one of the major components in tropospheric aerosols. It is not considered because there are no data of the complex refractive index in the infrared waveband of OC. There are also many types of OC, each of them has a different spectral signature. We assume, that the spectral signature of OC is very weak. However if there are spectral features which are not fitted, e.g. due to the presence of aerosol types not accounted for in the scattering database, the error margin on the retrieved aerosol types will be increased.

In conclusion, when aerosol is present in the atmosphere, the emission from aerosol can be measured by FTS. According to forward model simulations, different aerosol types show their own features~~and are independent of each other~~. Using artificial spectra with preset values, ~~the retrieval results are consistent with preset values under several possible perturbing scenery. Therefore, it is reliable to do aerosol components retrieval using the TCWret-V2~~error estimations caused by the retrieval could be calculated.

5 ~~Results~~

4.1 Aerosol-only Retrieval

On the 10$^{\mathrm{th}}$ of June 2020 ~~was an~~ there was a distinct aerosol event in Ny-Ålesund (compare Fig. 6, showing the aerosol distribution derived using the KARL Lidar). This aerosol event is chosen as our aerosol-only case. Figure ~~6~~ 7 presents the four

different aerosol classes and cloud based on the Lidar classification method (compare Sec.2.3). During this day, aerosols are mainly distributed below 1500 m (compare Fig. 6). From 7:00 to 11:00, the thickness of a coarse aerosol layer (dense aerosol in Lidar classification method in Sec. 2.3) near the surface decreases, while in the afternoon, this aerosol load increases and splits into two layers, one near the surface and another, activated aerosol, appears at the height of about 500 m. ~~Besides, there is a cloud signal~~ At around 8:00 ~~at the~~ clouds are present in a height of 3500 m, which has been screened out in the aerosol-only ~~retrieval in FTS~~ FTS retrieval.

~~Fig.~~Figure 7 shows the ~~result retrieved from~~ results retrieved from the FTS. From Fig. 7a, the dominant aerosol is sulfate above Ny-Ålesund, about AOD = 0.007 $\pm$ 0.0027 in daily average. ~~The other three aerosols also exist, but in much lower AOD values compared with~~ Dust also exists but lower than sulfate for most of the time, about AOD = 0.0039 $\pm$ 0.0029 for ~~dust daily average, AOD = 0.0017 $\pm$ 0.0007 for BC and AOD = 0.0012 $\pm$ 0.0002 for sea salt~~ daily average. The AOD of BC and sea salt are much lower than the reliable range of AOD, therefore, the retrieved values of BC and sea salt are not presented. From 9:00 to 11:00, the AOD of sulfate decreases with time~~and becomes similar to others at 11:00.~~ . After that, it increases slowly from 12:00 to 14:00, about 0.0135 at 14:00. ~~Besides, retrieval results also show that among the remaining three aerosols, Dust is dominant and the AOD of Dust increases slightly in the afternoon~~Compared with sulfate, dust as a second dominant aerosol does not show a significant daily variation as sulfate. From the long time period observation, dust and sulfate are independent in the retrieval (compare Fig. 9), which will be discussed in the following section. Considering the uncertainty of dust and the reliable range of the retrieval, it can be concluded that the AOD of dust is relatively stable during that day. From Fig. 7b, ~~sulfate, Dust and BC are small , about 0.3~~ both sulfate and dust are small in size, 0.25 $\pm$ 0.03 µm and 0.30 $\pm$ 0.06 µm, ~~while the size of Sea Salt is larger, about 0.8 , which is likely to originate locally rather than transported over long distances.~~ respectively.

Figure 8 shows the AOD from the FTS, AERONET and MERRA-2. In this analysis, the AOD from FTS will be called AOD_{IR}, the AOD from AERONET AOD_{AERO} and the AOD from MERRA-2 will be written as $AOD_{MERRA\text{-}2}$. From the measurement of ~~sun-photometer~~the Sun-photometer (AERONET), as shown in Fig. ~~A1~~8a, the AOD~~of aerosol~~ $_{AERO}$ (blue line for 500 nm and red line for 780 nm) decreases from 8:00 to 11:00 and increases after 14:24. ~~In Fig. 7a, the total AODin FTS also~~ Compared with AERONET, AOD_{IR} (black line) shows similar daily variation~~and is mainly caused by daily changes of sulfate~~, while the minimum in $AOD_{MERRA\text{-}2}$ (orange line) is at 08:00, about 3 hours earlier than AOD_{IR} and AOD_{AERO}. According to MERRA-2 reanalysis data, as shown in Fig. ~~A2~~A1b, the first two major aerosol components are sulfate and dust, which is consistent with AOD_{IR} in Fig. 8. Furthermore, the daily variation of $AOD_{MERRA\text{-}2}$ on the 10th of June 2020 is mainly caused by sulfate and sea salt. Apart from sea salt, which shows limited signal in the infrared waveband, the daily variation of sulfate in MERRA-2 is also ~~consistent with FTS measurement. The good agreement of FTS measurements with~~ similar to the FTS measurement, but the turning point in MERRA-2 is about 3 hours earlier than the one in the observations. In conclusion, the agreement of daily variation between FTS measurements and sun-photometer and the consistent in dominant aerosol components between FTS and MERRA-2 reanalysis data ~~shows~~ show the good quality in the retrieval results of FTS.

~~In~~ Additionally, in the afternoon, from Lidar measurement ~~, aerosols become activated~~ (compare Fig. 6), there are indications of activated aerosol at the height of about 500 m. ~~Since in~~ In the FTS retrieval algorithm, the databases of aerosol do not

include ~~the liquid water~~ liquid water or activated particles, which means only dry particles are considered in our retrieval. The appearance of an activated aerosol signal indicates that hygroscopic growth of aerosol ~~should~~ needs to be considered in the aerosol scattering properties look-up tables, which will be ~~established in the future~~the focus of future research.

4.2 ~~Cloud-only Retrieval~~Long Time period Observation

~~As we mentioned in Sec. 2.2, the intensity of emission spectra from thin clouds are very similar with those of aerosols. For showing the importance of Lidar measurement in the retrieval of FTS, a thin cloud-only case is selected and retrieved using two versions of retrieval algorithm.~~

~~Since aerosols are more or less present in the air~~ For continuous long-term observation of aerosols, Cloudnet (Illingworth et al., 2007) is a better alternative to the "KARL" Lidar measurement due to its improved data continuity and inclusion of aerosol height data and cloud type information. With the Cloudnet dataset, aerosol-only situations can be distinguished and the corresponding spectra are retrieved using TCWRET-V2. The results are presented in Fig. 9. The dominant aerosol type varies from April to August and is not fixed. For sulfate, it is ~~relatively hard to find a strictly cloud-only case. According to Lidar measurement on the 11th of June 2020, there was a thin cloud in Ny-Ålesund, as shown in Fig. 8. Limited by the number of observations in Lidar, we only get four Lidar measurements. Compared with cloud or other aerosol classes, we assume that spherical aerosol shows the weakest signal in FTS. Based on that, the time period when only thin clouds exists and aerosols are relatively negligible is about 10:22. Then, both TCWret V1 and V2 are used for gaining cloud parameters and aerosol parameters respectively to show the importance of prior Lidar classification information in retrieval.~~

~~Tab. **??** shows the results of cloud parameters using Tcwret V1 and aerosol parameters using Tcwret V2. From the cloud retrieval, there is a piece of ice cloud (τ =0.06433) on the 11th of June 2020. While from the aerosol retrieval, the signal of this thin ice cloud is misunderstood and retrieved as four aerosols. Without information from Lidar measurement, both retrievals are plausible. However, considering the Lidar as a reference, only cloud retrieval should be adopted, which means that the existence of clouds will interfere with the inversion of aerosols~~often present in the Arctic, higher during Spring time and lower in Summer. Similarly, BC is also frequently observed in the Arctic, with less obvious seasonal variations than that of sulfate. A BC outburst event is observed in each Spring and Summer. In Spring, sulfate and BC are significant while sea salt and dust are lower. In addition, a sea salt enhancement event is observed in Summer, which might be emitted from open water nearby. Fig. 9b - g present correlation plots between different aerosol types. None of them show a clear correlation, so they can be retrieved independent of each other.

5 Conclusions

An FTS instrument, NYAEM-FTS, for measuring down-welling emitted radiation is operated since 2019. Combining with the Raman-Lidar KARL, ~~the~~ aerosols can be observed more comprehensively than by either instrument alone.

For the FTS emission measurements, according to forward model simulation, the aerosol signatures of different aerosol types in the infrared ~~wavelength~~ spectral region are quite clear and independent. The retrieval algorithm ~~TCWret-V1~~ TCWRET-V1

(Richter et al., 2022) has been modified for retrieval of optical depth and R_{eff} of different aerosol types. Combined Lidar and FTS, a scheme of instruments joint measurement is designed and applied to do aerosol component retrieval. The measurements from both instruments in ~~two case studies are~~ a case study is analyzed on 10th of June 2020 (aerosol-only case) and on 11th of June 2020 (cloud-only case) to show the potential synergy.

In the aerosol-only case study, 10th of June 2020, the signal of cloud and aerosols could be distinguished clearly using measurements from the Lidar KARL. From the emission FTS measurement ~~, the~~ we see that sulfate is the dominant aerosol during the whole day. Comparing with sun-photometer measurements, the daily variation of aerosol AOD is mainly effected by sulfate in ~~infrared waveband~~the infrared. Comparing the results from NYAEM-FTS with MERRA-2 reanalysis data, the proportions of sulfate, dust and BC ~~also~~ show good agreement.

~~In the cloud-only case study, 11th of June~~ For long time period observations from April to August 2020, ~~Lidar could show the cloud or aerosol accurately and sensitively, giving a very good information on the state of the atmosphere. Without information from Lidar measurement, the signal of this thin ice cloud is retrieved as four aerosols from NYAEM-FTS measurements, which shows that the combination of both measurements is necessary~~sulfate is often present in the Arctic, higher during Spring time and relatively lower in Summer. Similarly, BC is also frequently observed in the Arctic, with less obvious seasonal variations than that of sulfate. During the Spring time, sulfate and BC are significant while sea salt and dust abundances are relatively low. None of them show a clear correlation, so they can be retrieved independent of each other.

The database used in ~~TCWret-V2~~ TCWRET-V2 does not include ~~wet~~ activated particles, which will be subject of a future study.

Code and data availability. The latest version of TCWRET can be downloaded from GitHub (https://github.com/RichterIUP/Total-Cloud-Water-retrieval). The Lidar data, spectra measured from the Emission FTS and retrieval resutls are available from the corresponding author upon request.

Appendix A: ~~Aerosol Optical Thickness~~ Description of the retrieval in ~~AERONET and MERRA-2~~TCWRET

~~The AERONET (AErosol RObotic NETwork) project is a federation of ground-based remote sensing aerosol networks. It is widely used as a ground-based reference for validation of aerosol retrievals. In Ny-Ålesund, a sun-photometer measuring solar extinction at several wavelengths is adopted to show the daily variance of AOD on 10th of June 2020, as shown in Fig. A1.~~

~~MERRA-2 (Modern-Era Retrospective analysis for Research and Applications version 2) is the latest version of global atmospheric reanalysis for the satellite era produced by NASA Global Modeling and Assimilation Office (GMAO) using the Goddard Earth Observing System Model (GEOS) version 5.12.4. M2T1NXAER is an hourly time-averaged 2-dimensional data collection in MERRA-2. This collection consists of assimilated aerosol diagnostics, such as column mass density of aerosol components (black carbon, dust, sea salt, sulfate, and organic carbon), surface mass concentration of aerosol components, and~~

total extinction (and scattering) AOD at 550 nm. The dataset covers the period of 1980 to present. Fig. A2 shows the AOD of sea salt, sulfate, dust and BC in Ny-Ålesund on 10th of June 2020.

Appendix B: Theory of Modified TCWret

The retrieval method adopted in modified TCWret for TCWRET for the aerosol case is the an optimal estimation method (Rodgers, 2000), the relationship between a measured emission spectrum y $\boldsymbol{y}$ and unknown aerosol state x $\boldsymbol{x}$ can be described by a simple mathematical model, as follows:

$$y\boldsymbol{y} = F(x)\boldsymbol{F}(\boldsymbol{x}) + \varepsilon\boldsymbol{\varepsilon} \tag{A1}$$

where $F(x)$ $\boldsymbol{F}(\boldsymbol{x})$ is the forward model and ε $\boldsymbol{\varepsilon}$ is the error of observation. The solution of the inverse problem is the state x $\boldsymbol{x}$ minimizing a cost function $\xi^2(x)$ $\boldsymbol{\xi^2}(\boldsymbol{x})$ usually defined as:

$$\xi^2(x)\boldsymbol{\xi^2}(\boldsymbol{x}) = [y - F(x)\boldsymbol{y} - \boldsymbol{F}(\boldsymbol{x})]^T S\mathbf{S}_y{}^{-1}[y - F(x)]^{-1}[\boldsymbol{y} - \boldsymbol{F}(\boldsymbol{x})] + [x\boldsymbol{x}_a - x - \boldsymbol{x}]S\mathbf{S}_a{}^{-1}[x_a - x]^{-1}[\boldsymbol{x}_a - \boldsymbol{x}] \tag{A2}$$

where S_y^{-1} $\mathbf{S}_y^{-1}$ is the inverse measurement error covariance matrix, containing the variances of the spectral radiance; x_a is the apriori; S_a^{-1} $\boldsymbol{x}_a$ is the a priori; $\mathbf{S}_a^{-1}$ is the inverse error of the a priori covariance matrix $x_a\boldsymbol{x}_a$; The state vector x in modified TCWret $\boldsymbol{x}$ in modified TCWRET is defined as follows:$x = (\tau_{seasalt}, \tau_{sulfate}, \tau_{dust}, \tau_{BC}, r_{seasalt}, r_{sulfate}, r_{dust}, r_{BC})$ $\boldsymbol{x} = (\tau_{seasalt}, \tau_{sulf}$ means AOD of aerosols, and r means R_{eff} of aerosols.

Since the forward model is a non-linear function, which means an iterative method is needed to minimize the cost function $\xi^2(x)\boldsymbol{\xi^2}(\boldsymbol{x})$, given as follow:

$$x\boldsymbol{x}_{n+1} = x\boldsymbol{x}_n + s\mathbf{s}_n \tag{A3}$$

Here x_n and x_{n+1} $\boldsymbol{x}_n$ and $\boldsymbol{x}_{n+1}$ are the aerosol parameters of the $n-th$ and $(n+1)-th$ step, and s_n $\mathbf{s}_n$ is the modification of the aerosol parameters during the $n-th$ iteration. For weak non-linear problems, the Gauss-Newton (GN) method can be successfully applied, while in significant non-linear situations, the GN method is not guaranteed to decrease the cost function, therefore the method of steepest descent could be used. The Levenberg-Marquardt method modification combines both methods by starting with the deepest descent method far away from the minimum and using the GN method near the minimum. At each iteration, a damping factor μ is adjusted in such a way that if the step results in a decrease in the cost-function, the damping factor μ is decreased, bringing the next step closer to the GN step. If the step causes the cost function to increase, the iteration is repeated with a higher damping factor μ, resulting in a step closer to the gradient descent direction Ceccherini and Ridolfi (2010). The adjustment vector s_n $\mathbf{s}_n$ could be determined by the governing equation, as follows:

$$(K\mathbf{K}_n^T S\mathbf{S}_y^{-1} K\mathbf{K}_n + S\mathbf{S}_a^{-1} + \mu^2 S\mathbf{S}_a^{-1})s\mathbf{s}_n = K\mathbf{K}_n^T S\mathbf{S}_y{}^{-1}[y - F(x_n)]^{-1}[\boldsymbol{y} - \boldsymbol{F}(\boldsymbol{x}_n)] + S\mathbf{S}_a^{-1} \cdot (x\boldsymbol{x}_a - x - \boldsymbol{x}_n) \tag{A4}$$

$K = (\frac{\partial F(x_i)_n}{\partial x_i})\mathbf{K} = (\frac{\partial \boldsymbol{F}(\boldsymbol{x}_i)_n}{\partial \boldsymbol{x}_i})$ is the jacobian matrix, i means parameters in the state vactor; $S_y^{-1} = diag(\sigma_i^{-1})$ $\mathbf{S}_y^{-1} = diag(\boldsymbol{\sigma}_i^{-1})$ is the inverse measurement error covariance matrix, containing the variances of the spectral radiance; x_a is the apriori; S_a^{-1} $\boldsymbol{x}_a$

is the a priori; $\mathbf{S}_a^{-1}$ is the inverse error of the a priori covariance matrix ~~x_a; $\mu^2 \cdot S_a^{-1}$~~ $\boldsymbol{x}_a$; $\mu^2 \cdot \mathbf{S}_a^{-1}$ is the Levenberg-Marquardt (LM) term, as we mentioned before. ~~$F(x_i)$~~ $\boldsymbol{F}(\boldsymbol{x}_i)$ is the calculated spectral radiance and ~~y~~ $\boldsymbol{y}$ is the measured spectral radiance.

The iteration is said to have converged, if the cost function ~~ξ^2~~ $\boldsymbol{\xi}^2$ does not change anymore, i.e. the change in the cost function ~~ξ~~ $\boldsymbol{\xi}$ is below a threshold. This threshold is set 0.001 in this study, i.e. the iteration has converged if

$$\frac{\boldsymbol{\xi}^2(\boldsymbol{x}_{n+1}) - \boldsymbol{\xi}^2(\boldsymbol{x}_{n+1})}{\boldsymbol{\xi}^2(\boldsymbol{x}_n)} < 0.001 \tag{A5}$$

A0.1 Averaging Kernels

The averaging kernels are a useful diagnostic tool to characterize the solution of the retrieval. In ~~TCWret~~TCWRET, averaging kernels are calculated via

$$\boldsymbol{A}\mathbf{A} = \frac{\partial \boldsymbol{x}_r}{\partial \boldsymbol{x}} = \frac{\partial \boldsymbol{x}_r}{\partial \boldsymbol{y}} \frac{\partial \boldsymbol{y}}{\partial \boldsymbol{x}} = \boldsymbol{T}\mathbf{T}_r \cdot \boldsymbol{K}\mathbf{K}_r \tag{A6}$$

where ~~x_r~~ $\boldsymbol{x}_r$ is the retrieved state vector; ~~x~~ $\boldsymbol{x}$ is the true value of state vector; ~~T_r~~ $\mathbf{T}_r$ is the final transfer matrix ~~T and K_r~~ $\mathbf{T}$ and $\mathbf{K}_r$ is the final jacobian matrix. According to Ceccherini and Ridolfi (2010), the final transfer matrix could be calculated as follows:

$$\begin{cases} \mathbf{T}_0 = \mathbf{0} \\ \mathbf{T}_{n+1} = \mathbf{G}_n + (\mathbf{I} - \mathbf{G}_n\mathbf{K}_n - \mathbf{M}_n\mathbf{S}_a^{-1})\mathbf{T}_n \\ \mathbf{G}_n = \mathbf{M}_n\mathbf{K}_n^T\mathbf{S}_y^{-1} \\ \mathbf{M}_n = (\mathbf{K}_n^T\mathbf{S}_y^{-1}\mathbf{K}_n + \mathbf{S}_a^{-1} + \mu^2\mathbf{D}_n)^{-1} \end{cases} \tag{A7}$$

where $\mathbf{0}$ is a zero matrix and $\mathbf{I}$ is an identity matrix, other quantities are described before. The matrices ~~K_n~~ $\mathbf{K}_n$ are calculated in Eq. A4. The calculation of the transfer matrix is performed in parallel to the minimisation. An example of averaging kernels is given as follows:

$$\boldsymbol{A} = \begin{array}{c} \begin{array}{cccccccc} \tau_{SS} & \tau_{SO4} & \tau_{Dust} & \tau_{BC} & Reff_{SS} & Reff_{SO4} & Reff_{Dust} & Reff_{BC} \end{array} \\ \begin{pmatrix} 0.280 & -0.099 & 0.264 & 0.232 & 0.093 & -0.046 & 0.014 & 0.073 \\ -0.057 & 0.940 & 0.047 & 0.042 & -0.067 & 0.057 & 0.026 & 0.020 \\ 0.006 & 0.006 & 0.585 & 0.036 & -0.007 & -0.040 & 0.151 & -0.022 \\ 0.172 & 0.178 & 0.163 & 0.171 & 0.030 & -0.011 & 0.023 & 0.065 \\ 0.248 & -0.134 & 0.268 & 0.250 & 0.112 & -0.042 & 0.075 & 0.063 \\ 0.000 & 0.000 & 0.000 & 0.000 & 0.000 & 0.000 & 0.000 & 0.000 \\ 0.012 & 0.025 & 1.354 & 0.102 & -0.023 & -0.075 & 0.414 & -0.051 \\ 0.149 & 0.177 & 0.195 & 0.190 & 0.045 & -0.014 & 0.062 & 0.061 \end{pmatrix} \end{array} \begin{array}{c} \tau_{SS} \\ \tau_{SO4} \\ \tau_{Dust} \\ \tau_{BC} \\ Reff_{SS} \\ Reff_{SO4} \\ Reff_{Dust} \\ Reff_{BC} \end{array}$$

The averaging kernels belong to the retrieved result, because they include much information about the retrieval results, e.g. how much influence is exerted by the a priori and how independent the retrieved quantities are from each other. On the diagonal elements one finds the derivatives of each element in the retrieved state vector with respect to its corresponding element in the true state vector. From the averaging kernel, the AOD of sulfate is the parameter least dependent on a priori information, followed by the AOD of dust and sea salt. Except for dust, all other aerosol size information is difficult to be retrieved. Besides, the information in each row or column suggests that there is very little connection between the parameters and that they are all independent of each other, supporting the finding of the low linear correlation coefficient (compare sec. 4.2).

Author contributions. PR implemented TCWRET and DJ developed it into the retrieval of aerosol parameters using TCWRET. MP designed and built the measurement setup, performed measurements and gave advice in the development of TCWRET. CR performed Lidar measurements and gave advice in using the Lidar data and the sun-photometer data. XS gave advice in forward model simulation. MB gave advice on the calibration processes, performed the measurements and maintained the instrument. JN gave advice in the setup of the measurement and the development of TCWRET. All authors contributed to the manuscript.

Competing interests. The authors declare no competing interests

Acknowledgements. We gratefully acknowledge ~~funding from~~ the funding by the Deutsche Forschungsgemeinschaft (DFG, German Research Foundation) –Project nummer 268020496 – TRR 172 , within the Transregional Collaborative Research ~~Centre TR 172 – Arctic~~ Center "ArctiC Amplification: Climate Relevant Atmospheric and ~~Surface Processes~~SurfaCe Processes, and Feedback Mechanisms ((AC)^3)~~, project~~ ", in sub-project E02: Ny-Ålesund Column Thermodynamic Structure, Clouds, Aerosols, Trace Gases and Radiative Effects. We thank the AWI Bremerhaven and the AWI Potsdam for logistical support on the AWIPEV research base and the station personnel for on-site support. We thank he senate of Bremen for partial funding of this work.

References

Abbatt, J. P. D., Leaitch, W. R., Aliabadi, A. A., Bertram, A. K., Blanchet, J.-P., Boivin-Rioux, A., Bozem, H., Burkart, J., Chang, R. Y. W., Charette, J., Chaubey, J. P., Christensen, R. J., Cirisan, A., Collins, D. B., Croft, B., Dionne, J., Evans, G. J., Fletcher, C. G., Galí, M., Ghahremaninezhad, R., Girard, E., Gong, W., Gosselin, M., Gourdal, M., Hanna, S. J., Hayashida, H., Herber, A. B., Hesaraki, S., Hoor, P., Huang, L., Hussherr, R., Irish, V. E., Keita, S. A., Kodros, J. K., Köllner, F., Kolonjari, F., Kunkel, D., Ladino, L. A., Law, K., Levasseur, M., Libois, Q., Liggio, J., Lizotte, M., Macdonald, K. M., Mahmood, R., Martin, R. V., Mason, R. H., Miller, L. A., Moravek, A., Mortenson, E., Mungall, E. L., Murphy, J. G., Namazi, M., Norman, A.-L., O'Neill, N. T., Pierce, J. R., Russell, L. M., Schneider, J., Schulz, H., Sharma, S., Si, M., Staebler, R. M., Steiner, N. S., Thomas, J. L., von Salzen, K., Wentzell, J. J. B., Willis, M. D., Wentworth, G. R., Xu, J.-W., and Yakobi-Hancock, J. D.: Overview paper: New insights into aerosol and climate in the Arctic, Atmos. Chem. Phys., 19, 2527–2560, https://doi.org/10.5194/acp-19-2527-2019, 2019.

Asmi, E., Kondratyev, V., Brus, D., Laurila, T., Lihavainen, H., Backman, J., Vakkari, V., Aurela, M., Hatakka, J., Viisanen, Y., Uttal, T., Ivakhov, V., and Makshtas, A.: Aerosol size distribution seasonal characteristics measured in Tiksi, Russian Arctic, Atmos. Chem. Phys., 16, 1271–1287, https://doi.org/10.5194/acp-16-1271-2016, 2016.

Bond, T. C., Doherty, S. J., Fahey, D. W., Forster, P. M., Berntsen, T., DeAngelo, B. J., Flanner, M. G., Ghan, S., Kärcher, B., Koch, D., et al.: Bounding the role of black carbon in the climate system: A scientific assessment, J. Geophys. Res.: Atmos., 118, 5380–5552, https://doi.org/10.1002/jgrd.50171, 2013.

Bony, S., Colman, R., Kattsov, V. M., Allan, R. P., Bretherton, C. S., Dufresne, J.-L., Hall, A., Hallegatte, S., Holland, M. M., Ingram, W., Randall, D. A., Soden, B. J., Tselioudis, G., and Webb, M. J.: How Well Do We Understand and Evaluate Climate Change Feedback Processes?, J. Clim., 19, 3445 – 3482, https://doi.org/10.1175/JCLI3819.1, 2006.

Boyer, M., Aliaga, D., Pernov, J. B., Angot, H., Quéléver, L. L. J., Dada, L., Heutte, B., Dall'Osto, M., Beddows, D. C. S., Brasseur, Z., Beck, I., Bucci, S., Duetsch, M., Stohl, A., Laurila, T., Asmi, E., Massling, A., Thomas, D. C., Nøjgaard, J. K., Chan, T., Sharma, S., Tunved, P., Krejci, R., Hansson, H. C., Kulmala, M., Petäjä, T., Sipilä, M., Schmale, J., and Jokinen, T.: A full year of aerosol size distribution data from the central Arctic under an extreme positive Arctic Oscillation: Insights from the MOSAiC expedition, Atmos. Chem. Phys. Discuss., 2022, 1–45, https://doi.org/10.5194/acp-2022-591, 2022.

Ceccherini, S. and Ridolfi, M.: Technical Note: Variance-covariance matrix and averaging kernels for the Levenberg-Marquardt solution of the retrieval of atmospheric vertical profiles, Atmos. Chem. Phys., 10, 3131–3139, https://doi.org/10.5194/acp-10-3131-2010, 2010.

Chang, H.-c. and Charalampopoulos, T.: Determination of the wavelength dependence of refractive indices of flame soot, Proc. R. Soc. London, Ser. A, 430, 577–591, https://doi.org/10.1098/rspa.1990.0107, 1990.

Clough, S., Shephard, M., Mlawer, E., Delamere, J., Iacono, M., Cady-Pereira, K., Boukabara, S., and Brown, P.: Atmospheric radiative transfer modeling: a summary of the AER codes, J. Quant. Spectrosc. Radiat. Transfer, 91, 233–244, https://doi.org/https://doi.org/10.1016/j.jqsrt.2004.05.058, 2005.

Domine, F., Sparapani, R., Ianniello, A., and Beine, H. J.: The origin of sea salt in snow on Arctic sea ice and in coastal regions, Atmos. Chem. Phys., 4, 2259–2271, https://doi.org/10.5194/acp-4-2259-2004, 2004.

Donth, T., Jäkel, E., Ehrlich, A., Heinold, B., Schacht, J., Herber, A., Zanatta, M., and Wendisch, M.: Combining atmospheric and snow radiative transfer models to assess the solar radiative effects of black carbon in the Arctic, Atmos. Chem. Phys., 20, 8139–8156, https://doi.org/10.5194/acp-20-8139-2020, 2020.

Eldridge, J. and Palik, E. D.: - Sodium Chloride (NaCl), in: Handbook of Optical Constants of Solids, edited by Palik, E. D., pp. 775–793, Academic Press, Burlington, https://doi.org/https://doi.org/10.1016/B978-012544415-6.50041-8, 1997.

Francis, D., Eayrs, C., Chaboureau, J.-P., Mote, T., and Holland, D. M.: Polar jet associated circulation triggered a Saharan cyclone and derived the poleward transport of the African dust generated by the cyclone, J. Geophys. Res.: Atmos., 123, 11–899, https://doi.org/10.1029/2018JD029095, 2018.

Francis, D., Eayrs, C., Chaboureau, J.-P., Mote, T., and Holland, D. M.: A meandering polar jet caused the development of a Saharan cyclone and the transport of dust toward Greenland, Advances in Science and Research, 16, 49–56, https://doi.org/10.5194/asr-16-49-2019, 2019.

Freudenthaler, V., Esselborn, M., Wiegner, M., Heese, B., Tesche, M., Ansmann, A., Müller, D., Althausen, D., Wirth, M., Fix, A., Ehret, G., Knippertz, P., Toledano, C., Gasteiger, J., Garhammer, M., and Seefeldner, M.: Depolarization ratio profiling at several wavelengths in pure Saharan dust during SAMUM 2006, Tellus B, 61, 165–179, https://doi.org/10.1111/j.1600-0889.2008.00396.x, 2009.

Gelaro, R., McCarty, W., Suárez, M. J., Todling, R., Molod, A., Takacs, L., Randles, C. A., Darmenov, A., Bosilovich, M. G., Reichle, R., Wargan, K., Coy, L., Cullather, R., Draper, C., Akella, S., Buchard, V., Conaty, A., da Silva, A. M., Gu, W., Kim, G.-K., Koster, R., Lucchesi, R., Merkova, D., Nielsen, J. E., Partyka, G., Pawson, S., Putman, W., Rienecker, M., Schubert, S. D., Sienkiewicz, M., and Zhao, B.: The Modern-Era Retrospective Analysis for Research and Applications, Version 2 (MERRA-2), J. Clim., 30, 5419 – 5454, https://doi.org/10.1175/JCLI-D-16-0758.1, 2017.

Graversen, R. G., Langen, P. L., and Mauritsen, T.: Polar Amplification in CCSM4: Contributions from the Lapse Rate and Surface Albedo Feedbacks, J. Clim., 27, 4433 – 4450, https://doi.org/10.1175/JCLI-D-13-00551.1, 2014.

Hersbach, H., Bell, B., Berrisford, P., Biavati, G., Horányi, A., Muñoz Sabater, J., Nicolas, J., Peubey, C., Radu, R., Rozum, I., Schepers, D., Simmons, A., Soci, C., Dee, D., and Thépaut, J.-N.: ERA5 hourly data on pressure levels from 1979 to present, Copernicus climate change service (c3s) climate data store (cds). (Accessed on < 01-12-2022 >), 10, https://doi.org/10.24381/cds.bd0915c6, 2018.

Illingworth, A. J., Hogan, R. J., E., O., Bouniol, D., Brooks, M. E., Delanoé, J., Donovan, D. P., Eastment, J. D., Gaussiat, N., Goddard, J. W. F., Haeffelin, M., Baltink, H. K., Krasnov, O. A., Pelon, J., Piriou, J.-M., Protat, A., Russchenberg, H. W. J., Seifert, A., Tompkins, A. M., van Zadelhoff, G.-J., Vinit, F., Willén, U., Wilson, D. R., and Wrench, C. L.: Cloudnet: Continuous Evaluation of Cloud Profiles in Seven Operational Models Using Ground-Based Observations, Bull. Am. Meteorol. Soc., 88, 883–898, 2007.

Koch, D., Bauer, S. E., Genio, A. D., Faluvegi, G., McConnell, J. R., Menon, S., Miller, R. L., Rind, D., Ruedy, R., Schmidt, G. A., and Shindell, D.: Coupled Aerosol-Chemistry–Climate Twentieth-Century Transient Model Investigation: Trends in Short-Lived Species and Climate Responses, J. Clim., 24, 2693 – 2714, https://doi.org/10.1175/2011JCLI3582.1, 2011.

Kodros, J. K., Hanna, S. J., Bertram, A. K., Leaitch, W. R., Schulz, H., Herber, A. B., Zanatta, M., Burkart, J., Willis, M. D., Abbatt, J. P. D., and Pierce, J. R.: Size-resolved mixing state of black carbon in the Canadian high Arctic and implications for simulated direct radiative effect, Atmos. Chem. Phys., 18, 11 345–11 361, https://doi.org/10.5194/acp-18-11345-2018, 2018.

Krinner, G., Boucher, O., and Balkanski, Y.: Ice-free glacial northern Asia due to dust deposition on snow, Climate Dynamics, 27, 613–625, https://doi.org/10.1007/s00382-006-0159-z, 2006.

Lee, S.-M., Shi, H., Sohn, B.-J., Gasiewski, A. J., Meier, W. N., and Dybkjær, G.: Winter Snow Depth on Arctic Sea Ice From Satellite Radiometer Measurements (2003–2020): Regional Patterns and Trends, Geophys. Res. Lett., 48, e2021GL094 541, https://doi.org/https://doi.org/10.1029/2021GL094541, e2021GL094541 2021GL094541, 2021.

May, N., Quinn, P., McNamara, S., and Pratt, K.: Multiyear study of the dependence of sea salt aerosol on wind speed and sea ice conditions in the coastal Arctic, J. Geophys. Res.: Atmos., 121, 9208–9219, https://doi.org/10.1002/2016JD025273, 2016.

Ming, J., Xiao, C., Cachier, H., Qin, D., Qin, X., Li, Z., and Pu, J.: Black Carbon (BC) in the snow of glaciers in west China and its potential effects on albedos, Atmos. Res., 92, 114–123, https://doi.org/https://doi.org/10.1016/j.atmosres.2008.09.007, 2009.

Mishchenko, M. I., Dlugach, J. M., Yanovitskij, E. G., and Zakharova, N. T.: Bidirectional reflectance of flat, optically thick particulate layers: an efficient radiative transfer solution and applications to snow and soil surfaces, Journal of Quantitative Spectroscopy and Radiative Transfer, 63, 409–432, https://doi.org/https://doi.org/10.1016/S0022-4073(99)00028-X, 1999.

Palik, E. D.: - Gallium Arsenide (GaAs), in: Handbook of Optical Constants of Solids, edited by Palik, E. D., pp. 429–443, Academic Press, Burlington, https://doi.org/https://doi.org/10.1016/B978-012544415-6.50018-2, 1997.

Park, J., Dall'Osto, M., Park, K., Gim, Y., Kang, H. J., Jang, E., Park, K.-T., Park, M., Yum, S. S., Jung, J., Lee, B. Y., and Yoon, Y. J.: Shipborne observations reveal contrasting Arctic marine, Arctic terrestrial and Pacific marine aerosol properties, Atmos. Chem. Phys., 20, 5573–5590, https://doi.org/10.5194/acp-20-5573-2020, 2020.

Philipp, D., Stengel, M., and Ahrens, B.: Analyzing the Arctic Feedback Mechanism between Sea Ice and Low-Level Clouds Using 34 Years of Satellite Observations, J. Clim., 33, 7479 – 7501, https://doi.org/10.1175/JCLI-D-19-0895.1, 2020.

Previdi, M., Smith, K. L., and Polvani, L. M.: Arctic amplification of climate change: a review of underlying mechanisms, Environ. Res. Lett., 16, 093 003, https://doi.org/10.1088/1748-9326/ac1c29, 2021.

Rathke, C. and Fischer, J.: Retrieval of Cloud Microphysical Properties from Thermal Infrared Observations by a Fast Iterative Radiance Fitting Method, J. Atmos. Ocean. Tech., 17, 1509 – 1524, https://doi.org/10.1175/1520-0426(2000)017<1509:ROCMPF>2.0.CO;2, 2000.

Rathke, C., Notholt, J., Fischer, J., and Herber, A.: Properties of coastal Antarctic aerosol from combined FTIR spectrometer and sun photometer measurements, Geophys. Res. Lett., 29, 46–1, https://doi.org/10.1029/2002GL015395, 2002.

Ren, L., Yang, Y., Wang, H., Zhang, R., Wang, P., and Liao, H.: Source attribution of Arctic black carbon and sulfate aerosols and associated Arctic surface warming during 1980–2018, Atmos. Chem. Phys., 20, 9067–9085, https://doi.org/10.5194/acp-20-9067-2020, 2020.

Revercomb, H. E., Buijs, H., Howell, H. B., LaPorte, D. D., Smith, W. L., and Sromovsky, L. A.: Radiometric calibration of IR Fourier transform spectrometers: solution to a problem with the High-Resolution Interferometer Sounder, Appl. Opt., 27, 3210–3218, https://doi.org/10.1364/AO.27.003210, 1988.

Richter, P., Palm, M., Weinzierl, C., Griesche, H., Rowe, P. M., and Notholt, J.: A dataset of microphysical cloud parameters, retrieved from Fourier-transform infrared (FTIR) emission spectra measured in Arctic summer 2017, Earth Syst. Sci. Data, 14, 2767–2784, https://doi.org/10.5194/essd-14-2767-2022, 2022.

Ritter, C., Neuber, R., Schulz, A., Markowicz, K., Stachlewska, I., Lisok, J., Makuch, P., Pakszys, P., Markuszewski, P., Rozwadowska, A., Petelski, T., Zielinski, T., Becagli, S., Traversi, R., Udisti, R., and Gausa, M.: 2014 iAREA campaign on aerosol in Spitsbergen – Part 2: Optical properties from Raman-lidar and in-situ observations at Ny-Ålesund, Atmospheric Environment, 141, 1–19, https://doi.org/https://doi.org/10.1016/j.atmosenv.2016.05.053, 2016.

Rodgers, C. D.: Inverse methods for atmospheric sounding: theory and practice, vol. 2, World scientific, 2000.

Rowe, P. M., Neshyba, S., and Walden, V. P.: Radiative consequences of low-temperature infrared refractive indices for supercooled water clouds, Atmos. Chem. Phys., 13, 11 925–11 933, https://doi.org/10.5194/acp-13-11925-2013, 2013.

Schmale, J., Zieger, P., and Ekman, A. M.: Aerosols in current and future Arctic climate, Nat. Clim. Change, 11, 95–105, https://doi.org/10.1038/s41558-020-00969-5, 2021.

Schmeisser, L., Backman, J., Ogren, J. A., Andrews, E., Asmi, E., Starkweather, S., Uttal, T., Fiebig, M., Sharma, S., Eleftheriadis, K., Vratolis, S., Bergin, M., Tunved, P., and Jefferson, A.: Seasonality of aerosol optical properties in the Arctic, Atmos. Chem. Phys., 18, 11 599–11 622, https://doi.org/10.5194/acp-18-11599-2018, 2018.

Schulz, H., Zanatta, M., Bozem, H., Leaitch, W. R., Herber, A. B., Burkart, J., Willis, M. D., Kunkel, D., Hoor, P. M., Abbatt, J. P. D., and Gerdes, R.: High Arctic aircraft measurements characterising black carbon vertical variability in spring and summer, Atmos. Chem. Phys., 19, 2361–2384, https://doi.org/10.5194/acp-19-2361-2019, 2019.

Serreze, M. C. and Barry, R. G.: Processes and impacts of Arctic amplification: A research synthesis, Global and Planetary Change, 77, 85–96, https://doi.org/https://doi.org/10.1016/j.gloplacha.2011.03.004, 2011.

Shaw, G. E.: The Arctic Haze Phenomenon, Bull. Am. Meteorol. Soc., 76, 2403 – 2414, https://doi.org/10.1175/1520-0477(1995)076<2403:TAHP>2.0.CO;2, 1995.

Soden, B. J. and Held, I. M.: An Assessment of Climate Feedbacks in Coupled Ocean–Atmosphere Models, J. Clim., 19, 3354 – 3360, https://doi.org/10.1175/JCLI3799.1, 2006.

Stamnes, K., Tsay, S.-C., Wiscombe, W., and Jayaweera, K.: Numerically stable algorithm for discrete-ordinate-method radiative transfer in multiple scattering and emitting layered media, Appl. Opt., 27, 2502–2509, https://doi.org/10.1364/AO.27.002502, 1988.

Struthers, H., Ekman, A. M. L., Glantz, P., Iversen, T., Kirkevåg, A., Mårtensson, E. M., Seland, Ø., and Nilsson, E. D.: The effect of sea ice loss on sea salt aerosol concentrations and the radiative balance in the Arctic, Atmos. Chem. Phys., 11, 3459–3477, https://doi.org/10.5194/acp-11-3459-2011, 2011.

Taylor, P. C., Cai, M., Hu, A., Meehl, J., Washington, W., and Zhang, G. J.: A Decomposition of Feedback Contributions to Polar Warming Amplification, J. Clim., 26, 7023 – 7043, https://doi.org/10.1175/JCLI-D-12-00696.1, 2013.

Turner, D. D.: Arctic Mixed-Phase Cloud Properties from AERI Lidar Observations: Algorithm and Results from SHEBA, J. Appl. Meteorol., 44, 427 – 444, https://doi.org/10.1175/JAM2208.1, 2005.

Turner, D. D.: Ground-based infrared retrievals of optical depth, effective radius, and composition of airborne mineral dust above the Sahel, J. Geophys. Res.: Atmos., 113, https://doi.org/https://doi.org/10.1029/2008JD010054, 2008.

Wagner, R., Kaufmann, J., Möhler, O., Saathoff, H., Schnaiter, M., Ullrich, R., and Leisner, T.: Heterogeneous Ice Nucleation Ability of NaCl and Sea Salt Aerosol Particles at Cirrus Temperatures, J. Geophys. Res.: Atmos., 123, 2841–2860, https://doi.org/https://doi.org/10.1002/2017JD027864, 2018.

Wendisch, M., Brückner, M., Burrows, J., Crewell, S., Dethloff, K., Ebell, K., Lüpkes, C., Macke, A., Notholt, J., Quaas, J., et al.: Understanding causes and effects of rapid warming in the Arctic, Eos, 98, https://doi.org/10.1029/2017EO064803, 2017.

Zanatta, M., Laj, P., Gysel, M., Baltensperger, U., Vratolis, S., Eleftheriadis, K., Kondo, Y., Dubuisson, P., Winiarek, V., Kazadzis, S., Tunved, P., and Jacobi, H.-W.: Effects of mixing state on optical and radiative properties of black carbon in the European Arctic, Atmos. Chem. Phys., 18, 14 037–14 057, https://doi.org/10.5194/acp-18-14037-2018, 2018.

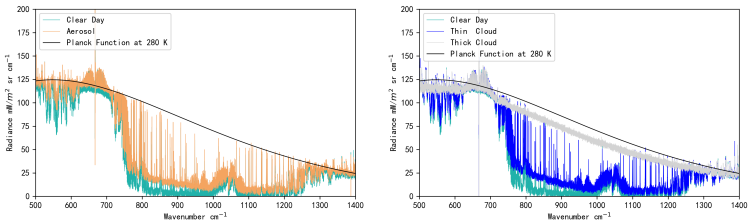

Figure 1. Four different emission spectra measured by NYAEM-FTS in clear sky (green), aerosol (yellow, left), thin cloud (blue, right) and thick cloud (gray, right) event respectively. The radiance calculated using Planck function at 280 K (black line) is presented in this figure. Note: the emission around 650 cm^{-1} ~~is~~ originates in ambient CO_2 from the laboratory air.

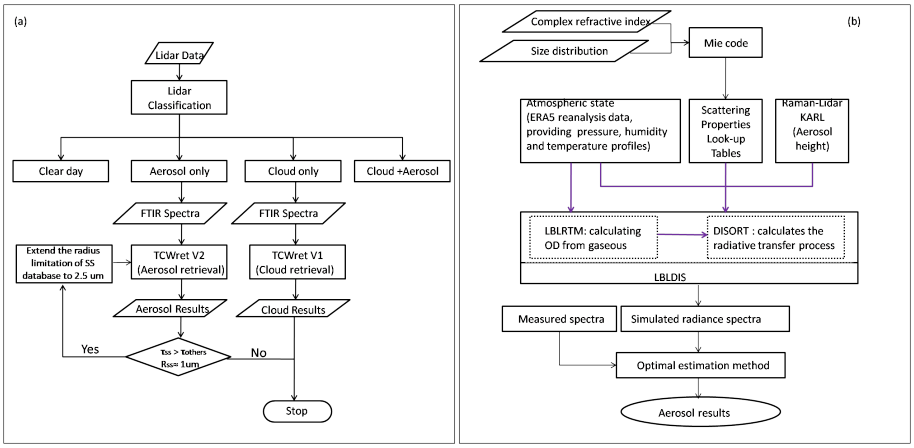

Figure 2. Instruments Joint Observation Scheme (a) and flow diagram of ~~TCWret-V2~~ TCWRET-V2 (b).

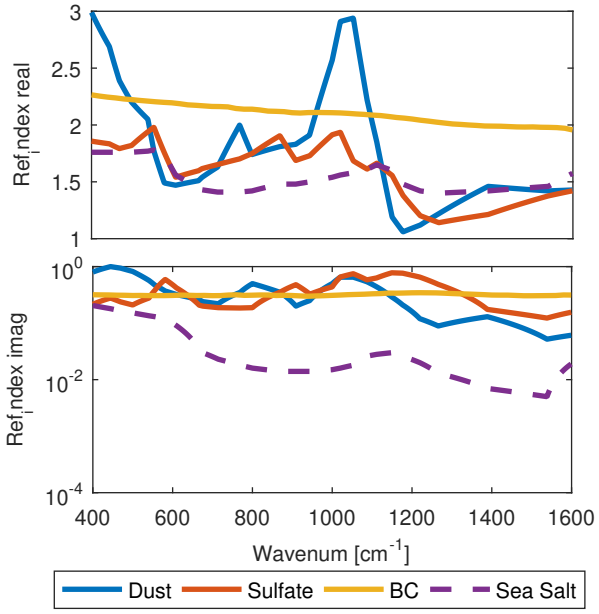

Figure 3. The complex refractive index of dust, sulfate, BC, and sea salt. The complex imaginary refractive index of sulfate and dust are based on OPAC/GADA database, BC from Chang and Charalampopoulos (1990), sea salt from Eldridge and Palik (1997), and Palik (1997). Those data have been downloaded from: http://eodg.atm.ox.ac.uk/ARIA/.

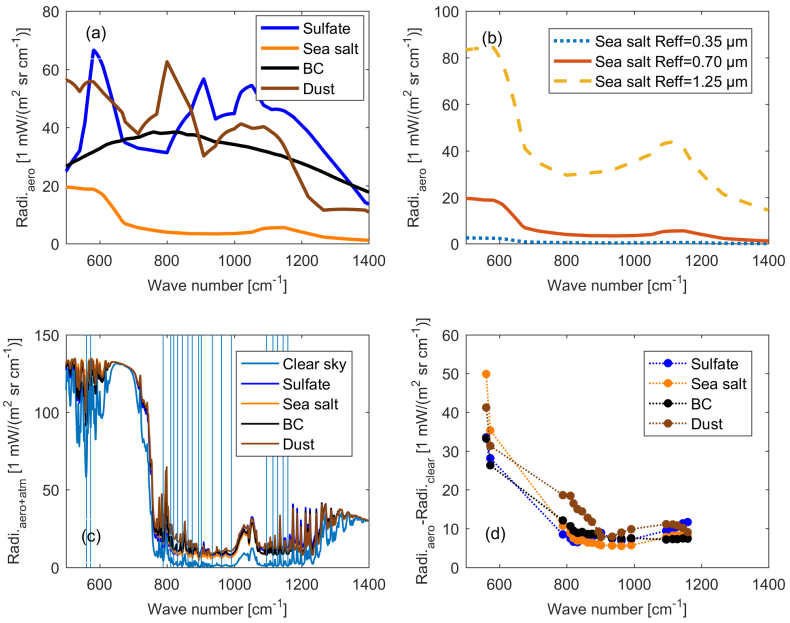

Figure 4. The emission spectra of small aerosol particles (dust in brown, sulfate in blue, sea salt in orange, BC in black) with Reff = 0.35 μm and number density = 2000 cm^{-3} (a); The emission spectra of sea salt with different particle sizes (b); The emission spectra of aerosols ($AOD_{900\ cm^{-1}}$ = 0.1) with atmosphere gases and clear sky case (c); The difference between total emission spectra of aerosol and clear sky case in micro windows (d). The vertical blue lines in (c) show the mid-values of micro windows selected for retrieval. The emission spectra are simulated from LBLDIS with the resolution of 1 cm^{-1}.

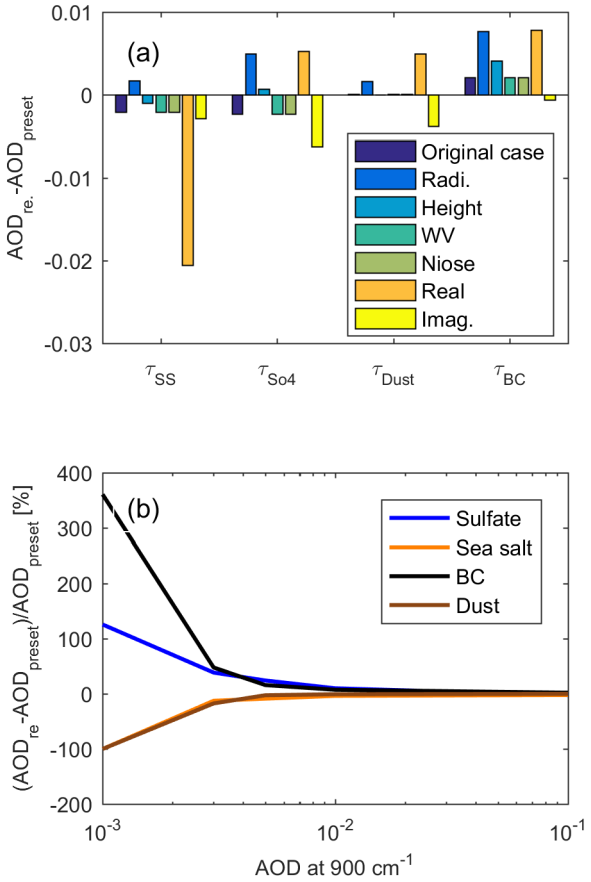

Figure 5. The difference between retrieved AOD in ~~orginal~~ original case and several possible perturbing scenery (compare Table 2.) with preset values (a). The relative uncertainties of AOD in original cases with several preset values (b). Note: The artificial spectra with several preset values in (b) means the AOD's of aerosols are set from 0.001 to 0.1. With the same method but for different preset AODs, the reliable range of AOD are given in (b).

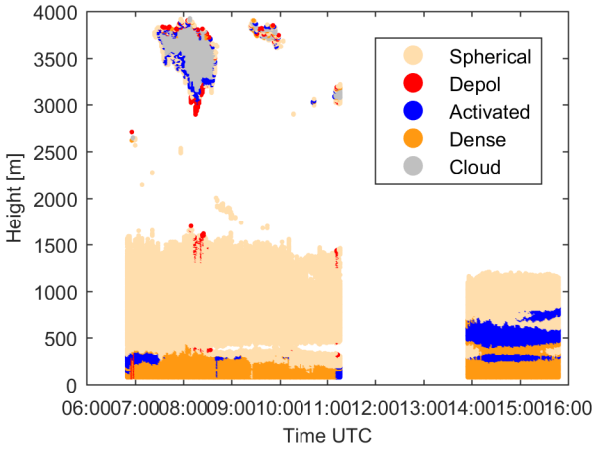

Figure 6. Four different aerosol classes (spherical particles in light yellow, depolarization particles in red, activated particles in blue, and dense particles in deep yellow) and cloud (gray) based on Lidar classification method on 10th of June 2020.

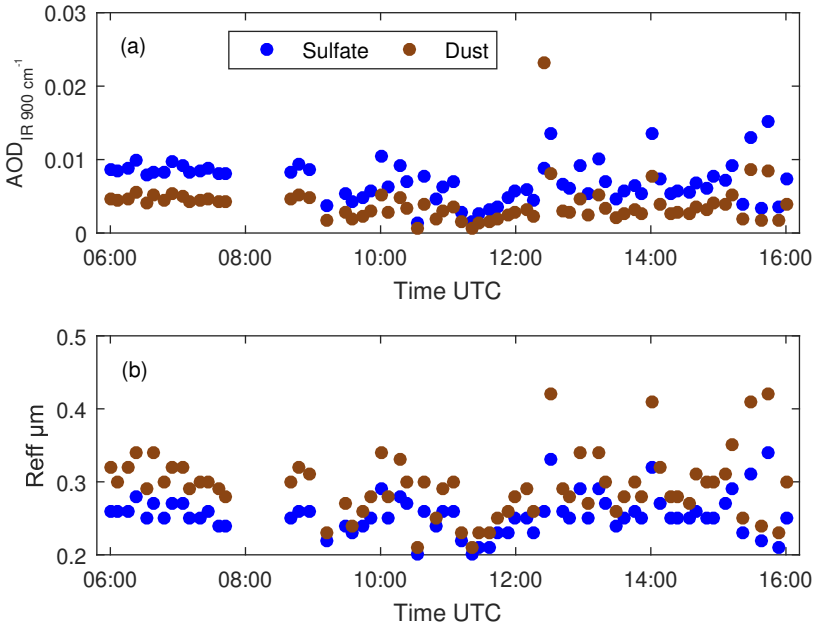

Figure 7. AOD of ~~sea salt (orange),~~ sulfate (blue) ~~,~~ and dust (brown) ~~, BC (black) and total AOD (black solid line)~~ retrieved from emission FTS measurements (a) and ~~Reff~~ R_{eff} results with same color information (b) on 10th of June 2020.

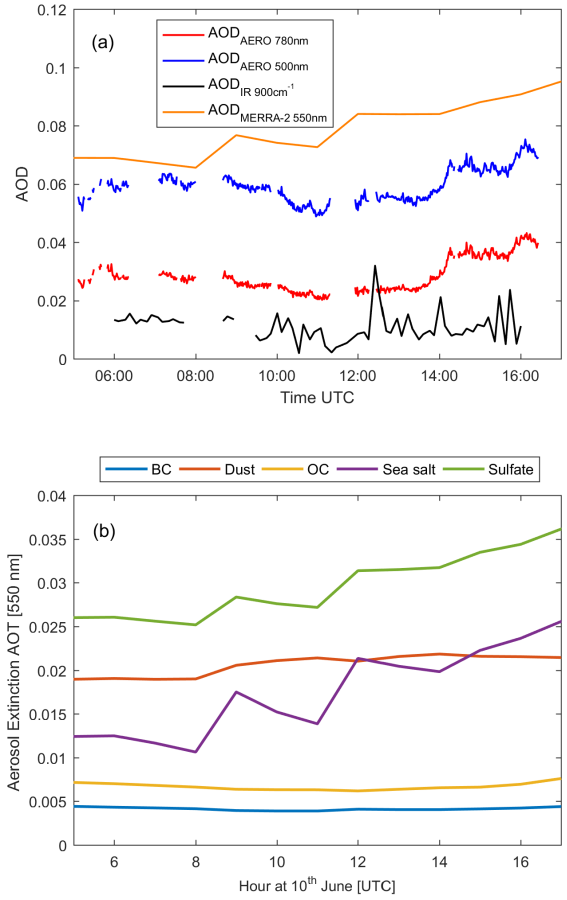

Figure 8. ~~Four different aerosol classes~~ AOD measured by Sun-photometer (~~spherical particles in light yellow, depolarization particles in red~~AERONET, ~~activated particles~~ 500 nm in blue ~~,~~ and ~~dense particles~~ 780 nm in ~~deep yellow~~red), AOD measured by FTS (900 cm^{-1} in black) and ~~cloud~~ AOD from MERRA-2 reanalysis data (~~gray~~550 nm) ~~based~~ in Ny-Ålesund on ~~Lidar classification method~~ 10th of June 2020 (a); AOD of different aerosol components in MERRA-2 reanalysis datain Ny-Ålesund on ~~11~~10th of June ~~2020.~~2020 (b). AERONET data from: https://www.mdpi.com/2072-4292/11/11/1362; MERRA-2 data from: https://goldsmr4.gesdisc.eosdis.nasa.gov/data/MERRA2/M2T1NXAER.5.12.4/.

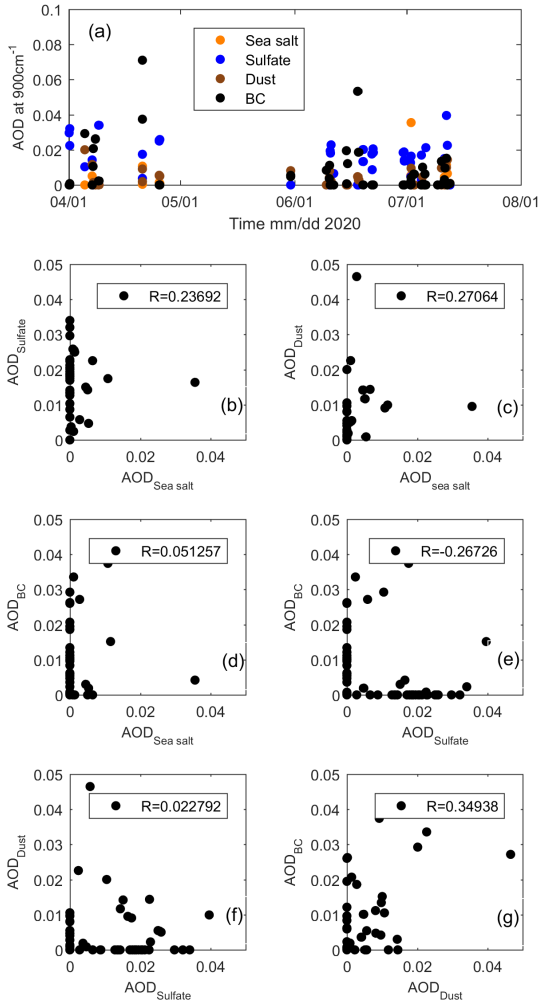

Figure 9. Long time period observation using FTS from April to August (a), The correlation between sea salt and sulfate (b); The correlation between sea salt and dust (c); The correlation between sea salt and BC (d); The correlation between sulfate and BC (e); The correlation between sulfate and dust (f); Th correlation between dust and BC (g).

Table 1. Aerosol classification by Lidar measurements as ~~give~~ given by Ritter et al. (2016)

Classes	$\beta_{532}^{aer}(Mm^{-1}sr^{-1})$	δ_{532}^{aer}	CR	Description
Clear day	$\beta < 0.4$	$\delta < 2.05\%$		Clear day
Clear depol.	β<0.4	$\delta \geq 2.05\%$		Clear day with polarized signal.
Spherical Aerosol	$0.4 \leq \beta < 1$	$\delta < 2.05\%$		Spherical fine particles, possibly from long-distance transportation, e.g. sulfate.
Depol. Aerosol	$0.4 \leq \beta < 1$	$\delta \geq 2.05\%$		Polarized fine particles with irregular shapes, e.g. dust.
Activated Aerosol	$1 \leq \beta \leq 3$	$\delta < 2.05\%$	$CR < 1.7$	Aerosol hygroscopic growth into larger size, e.g. sea salt, sulfates.
Dense Aerosol	$1 \leq \beta \leq 3$		$CR \geq 1.7$	Medium size aerosol, e.g. sea salt, dust.
Cloud	$\beta > 3$			Cloud

Table 2. Parameter errors and modifications in artificial spectra

Parameters	Modifications
Height of aerosol	+10% (200 m)
Water vapor profiles	-10%
Calibration error	+1 mW/sr*m2*cm-1
Measurement error	Normally distributed noise with mean value of 0 and variance of 1
Complex refractive index (real part)	-10%
Complex refractive index (imaginary part)	-10%

~~Cloud parameters and aerosol parameters using TCWret-V1 and TCWret-V2 on 11th of June 2020 Tcwret version $\tau_{Liquidcloud}\tau_{Icecloud}\tau_{S}$ V1 00.0643Tcwret V2 0.0002760.0004250.0002080.000219~~

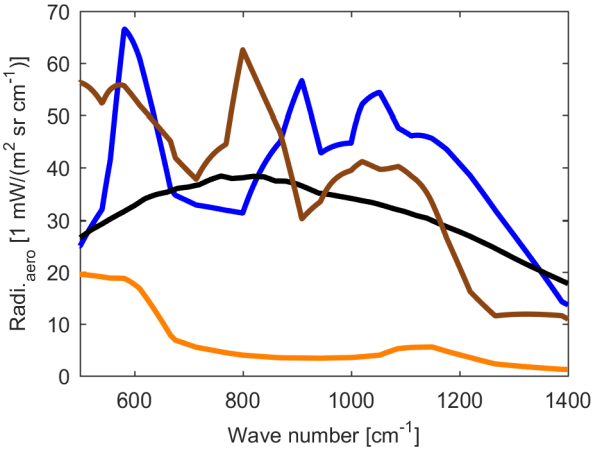

Figure A1. ~~Sun-photometer~~ The emission spectra of large aerosol ~~optical depth~~ particles (dust in ~~Ny-Ålesund on 10th of June 2020. From: https://aeronet.gsfc.nasa.gov/~~brown, sulfate in blue, sea salt in orange, BC in black) with Reff = 0.70 µm and number density = 2000 cm^{-3}.

Interval (cm^{-1})
558.5–562.0
571.0–574.0
785.9–790.7
809.5–813.5
815.3–824.4
828.3–834.6
842.8–848.1
860.1–864.0
872.2–877.5
891.9–895.8
898.2–905.4
929.6–939.7
959.9–964.3
985.0–991.5
1092.2–1098.1
1113.3–1116.6
1124.4–1132.6
1142.2–1148.0
1155.2–1163.4

Figure A2. ~~Merra-2 reanalysis aerosol data~~ Microwindows used in ~~Ny-Ålesund on 10th of June 2020.From: https://goldsmr4.gesdisc.eosdis.nasa.gov/data/MERRA2/M2T1NXAER.5.12.4/~~TCWRET to retrieve the microphysical aerosol or cloud parameters (Richter et al., 2022).